

# Observing complete gravitational wave signals from dynamical capture binaries

William E. East,<sup>1,\*</sup> Sean T. McWilliams,<sup>1,2,†</sup> Janna Levin,<sup>2,3</sup> and Frans Pretorius<sup>1</sup>

<sup>1</sup>*Department of Physics, Princeton University, Princeton, NJ 08544*

<sup>2</sup>*Institute for Strings, Cosmology and Astroparticle Physics, Columbia University, New York, NY 10027*

<sup>3</sup>*Department of Physics and Astronomy, Barnard College of Columbia University, 3009 Broadway, New York, NY 10027*

(Dated: September 9, 2022)

We present a model for the inspiral, merger, and ringdown of highly eccentric compact binaries. We map the binary to an effective single black hole system described by a Kerr metric, thereby including certain relativistic effects not incorporated in existing post-Newtonian approximations. The resultant geodesics source quadrupolar radiation and in turn are evolved under its dissipative effects. At the light ring, we attach a merger model that was previously developed for quasicircular mergers but also performs well for eccentric mergers with little modification. We apply our model to assess the detectability of these sources for initial, Enhanced, and Advanced LIGO across the parameter space of nonspinning close capture compact binaries. We conclude that, should these systems exist in nature, the vast majority will be missed by conventional burst searches or by quasicircular waveform templates in the advanced detector era. Other methods, such as eccentric templates or, more practically, a stacked excess power search, must be developed to avoid losing these sources. These systems would also have been missed frequently in the initial LIGO data analysis. Thus, previous null coincidence results with detected GRBs can not exclude the possibility of coincident gravitational wave signals from eccentric binaries.

PACS numbers: 95.30.Sf, 97.60.Lf

## I. INTRODUCTION

In dense stellar regions, such as galactic nuclei or globular clusters, individual black holes (BHs) or neutrons stars (NSs) can become gravitationally bound as energy is lost to gravitational radiation during a close passage. These dynamically captured pairs may be additional sources for gravitational-wave (GW) detectors, as well as sources of electromagnetic (EM) transients such as short gamma-ray bursts (SGRBs). Eccentric pairs will be distinguishable from quasicircular coeval binaries, which are born in a bound system and have had time to circularize before reaching the sensitive bandwidths of ground-based GW observatories such as LIGO [1], VIRGO [2], GEO600 [3] and KAGRA(LCGT) [4].

The primary purpose of this paper is to study the detectability of sources that retain eccentricity while in the LIGO band (for simplicity we only employ LIGO sensitivity curves). Before getting into the details of our model and results, we briefly review current event rate estimates, high-eccentricity population fractions, possible EM counterparts, and the GW detectability of dynamically captured compact objects.

### A. Event Rates

Galactic nuclei are a promising setting for the formation of dynamical capture binaries. Mass segregation

around a central massive BH can lead to large densities of stellar mass BHs and stars. For example, the Fokker-Planck model used in [5] suggests that our galactic nucleus should have  $\sim 2000$  BHs and  $\sim 400$  NSs in the central 0.1 pc. In [6, 7], the event rate for the formation of BH-BH binaries from GW capture in this setting was estimated to be roughly between  $0.01$ - $1.0 \text{ yr}^{-1} \text{ Gpc}^{-3}$ , with corresponding Advanced LIGO detection rates of  $\approx 1 - 10^2 \text{ yr}^{-1}$ . This rate assumes that the number density  $n$  of BHs in galactic nuclei has a scatter with  $\langle n^2 \rangle / \langle n \rangle^2 = 30$ . Assuming no scatter would reduce the above rate by a factor of 30. This also assumes a number density of contributing galaxies of  $0.05 \text{ Mpc}^{-3}$ , i.e. it includes all galaxies as contributing roughly equally. Lower mass galaxies are not as well understood, though if a significant number of them have total cluster mass fractions above the 2.5% used in the aforementioned calculation, this rate would increase. Other unaccounted for effects, such as steeper profiles from light-dominated mass functions [8], could also potentially increase this rate. The formation of BH-NS binaries is estimated to be  $\sim 1\%$  of this rate [6].

Dynamical capture binaries may also form in globular clusters (GCs) that undergo core-collapse [9, 10]. In [11] binary formation through tidal capture was studied. Using M15 as a prototypical GC, it was calculated that the NS-NS tidal capture rate would peak at  $\sim 50 \text{ yr}^{-1} \text{ Gpc}^{-3}$  at  $z = 0.7$  (falling to  $\sim 30 \text{ yr}^{-1} \text{ Gpc}^{-3}$  by  $z = 0$ ) for their default model of core-collapse. They also provide a scaling to BH-NS and BH-BH mergers which (assuming  $M_{\text{BH}} = 4.5 M_{\odot}$  and a relative fraction of BHs to NSs  $f_{\text{BH}}/f_{\text{NS}} \approx 0.28$ ) gives rates that peak at  $\sim 70 \text{ yr}^{-1} \text{ Gpc}^{-3}$  and  $\sim 20 \text{ yr}^{-1} \text{ Gpc}^{-3}$  for BH-NS and BH-BH mergers, respectively. This scaling does not in-

\*Electronic address: weast@princeton.edu

†Electronic address: stmcwill@princeton.edu

clude complications due to BH ejection [12–16]. Also, these calculations do not include the likely reduction in compact object (CO) populations within the GC due to natal kicks. In [17] it was found that including a 5% NS retention fraction when fitting simulation results to observations of M15, and assuming no central BH reduced the estimated number of NSs in the inner 0.2 pc by  $\sim 1/4$  compared to a similar study that did not include natal kicks [18]. The calculated NS-NS merger rate is quite sensitive to the fraction  $f$  of NSs in the core, scaling as  $\sim f^2$ , which means the aforementioned rates could be too large by an order of magnitude if retention rates are this low. However, observations suggest that in some GCs the NS retention fraction could be as high as 20% [19]. Also, note that the tidal capture cross section used in [11] is more than an order of magnitude smaller than the GW capture cross section (discussed in the following section) for compact objects, and using the latter would increase the rates by the same factor. In geometric units  $G = c = 1$  (which, unless otherwise stated, we use throughout), tidal capture is estimated to occur in [11] for periape values  $r_p/M \leq 32$ , 25, and 13 for NS-NS, BH-NS, and BH-BH binaries respectively.

In [20] NS-NS binary formation in GCs via exchange interactions was studied, giving a merger rate of  $\sim 2 \text{ yr}^{-1} \text{ Gpc}^{-3}$ . A similar mechanism was explored in [21] for BH-NS systems; the results depend sensitively on the initial mass fraction of BHs, with more massive BHs leading to higher event rates. For example, models where the GC contained  $M = 35_\odot$  BHs lead to advanced LIGO detection rates of  $0.04\text{--}0.7 \text{ yr}^{-1}$ . Though in contrast to tidal/GW capture discussed in the previous paragraph, the mechanisms looked at in both these studies typically produce binaries with periods of 0.1 days or longer, and they will effectively circularize before entering the LIGO band.

There is also the possibility that eccentric mergers could result from hierarchical triples though the Kozai mechanism. This has been suggested to occur in BH-BH mergers in GCs [16, 22, 23], CO mergers around supermassive BHs in galactic nuclei [24], as well as coeval or dynamically formed BH-NS or NS-NS binaries [25]. Though the dynamics of these systems will be different from those studied here, they could be similar at late times. Efforts to understand this mechanism in the general-relativistic regime are ongoing (see e.g. [26]) and the event rates of these systems are not well known (though see [27]).

## B. Cross Sections, High Eccentricity Fractions

We focus on mergers with initial periape  $r_p \lesssim 10M$ , where  $M$  is the total mass, making this study complementary to previous studies [6, 7]. As we show later, in this regime essentially all mergers occur with non-negligible eccentricity ( $e \gtrsim 0.2$ ). This is also the regime where strong-field effects such as black hole spin and

zoom whirl behavior can influence the dynamics. To estimate the fraction of dynamical capture binaries that retain high-eccentricity, we can use Newtonian dynamics with quadrupolar energy loss following [28–30]. First, for a hyperbolic orbit with a small velocity at infinity  $v \ll 1$ , the relationship between impact parameter  $b$  and  $r_p$  is  $r_p \approx b^2 v^2 / 2M$ . In other words, the cross section  $\sigma \propto b^2$  scales *linearly* with  $r_p$ . The maximum pericenter passage that leads to a bound system through gravitational radiation loss<sup>1</sup> is  $r_{p,m} \approx (31\eta)^{2/7} v^{-4/7} M$ , where  $\eta = m_1 m_2 / M^2 = q / (1 + q)^2$  is the symmetric mass ratio with  $q$  the mass ratio. For a galactic nuclear cluster where  $v \approx 1000 \text{ km/s}$ , between 20 – 30% of dynamical capture binaries (where the range is from  $q = 1$  to  $q = 0.1$ ) will have  $r_p/M < 10$ ; for a globular cluster with  $v \approx 10 \text{ km/s}$  this drops to 1.5 – 2.0%.

Although we focus on those with small initial periape, *all* dynamical capture binaries will have a repeated burst phase [7]. For a large fraction of expected binary masses the repeated bursts will be within the Advanced LIGO band. The burst frequency is  $\nu_b \approx r_p^{-1} (r_p/M)^{-1/2}$ ; the lowest frequency occurs at  $r_p = r_{p,m}$ , which ranges from  $(1 - 100\text{Hz})/M_{10}$  for  $q = 0.1$  encounters in globular clusters to  $q = 1$  encounters in nuclear clusters, with  $M_{10} = M/10M_\odot$ . To estimate the percentage of systems that will end with a low eccentricity inspiral phase, if the initial periape is  $r_{p,i}$ , and we consider the repeated burst phase to end at a periape of  $r_{p,f}$  with eccentricity  $e_f$ , from [29]  $r_{p,i} \approx 0.57 r_{p,f} (1 + e_f) e_f^{-12/19} [1 + O(e_f^2)]$ . For example, if a binary with  $e_f < 0.1$  by  $r_{p,f} = 10M$  can be considered to have of a low eccentricity inspiral phase, then this corresponds to all systems with  $r_{p,i} > 27M$ . For nuclear clusters, this is between 20 – 40% for  $q = 1 - 0.1$ , while the corresponding range for globular clusters is 94 – 96%.

## C. Electromagnetic Counterparts

Binary NS or BH-NS mergers are thought to be progenitors for SGRBs, and may also source a number of other EM transients [31, 32]. Possibilities include optical/UV emission on timescales of a day from radioactive decay of ejected material. (This depends on heavy element opacities. Recent work using more detailed calculations suggest the timescale may be up to a week with emission peaking in the IR [33]). Interaction of the outflow with surrounding matter can also produce radio emission on timescales of weeks to years [34]. And, for

<sup>1</sup> As mentioned earlier, for the COs considered here energy lost to tidal effects is much less than GW emission at these separations, so the latter process determines the cross section. Also, when a bound system is formed, the fraction that have a semi-major axis large enough to have the binary be tidally unbound by subsequent interaction with the surrounding cluster potential is insignificant.

binary NS mergers, strong shocks produced can emit in radio to X-rays over a second to day timescales [35].

Simulations of eccentric BH-NS and NS-NS mergers have shown a rich variation in outcome with impact parameter, with the possibility of large accretion disks as well as ejecta that could undergo the r-process [11, 36–39]. There is also significant variability in observed SGRBs. It is not implausible that this may in part be due to a sub-class of SGRBs associated with dynamical capture binaries. Though not conclusive, there is also observational evidence for multiple SGRB progenitors. Of SGRBs with identified host galaxies,  $\sim 25\%$  have offsets of  $\gtrsim 15$  kpc from their hosts [40], which would be consistent with kicked, primordially formed binary COs or with dynamically formed binaries in globular clusters. The latter may be preferred for the largest offsets [41], especially if primordial binary COs experience weak kicks [42]. X-ray afterglows suggests that different progenitors may be responsible for SGRBs with and without extended emission [43]; simulations of dynamical capture binaries show it is more common to get long tidal tails, which could lead to extended emission as the material falls back to the accretion disk. There is also a claim that a high-energy gamma-ray source observed in Terzan 5 may be the remnant of a binary CO merger-powered SGRB [44]; if true, this provides evidence that dense cluster environments can be significant sources of binary CO mergers.

The timescales between close encounters in eccentric mergers may also explain observed delays between precursors and SGRBs [45]. For example, NS crust cracking on a non-merging close encounter could potentially cause flares that precede the merger by an interval ranging from milliseconds to possibly a few seconds [38].

#### D. Gravitational Wave Detectability

Multimessenger exploration is of course an exciting possibility. Even a null GW detection provides astronomical information as it rules out compact object mergers as the source of an observed GRB, but only if the detectability of these types of signals is understood. Given the disparate nature of the waves from dynamical capture vs coeval mergers, data analysis methods designed specifically for each are required for this kind of astronomy. Methods to search for quasicircular inspiral (of relevance to the majority of coeval binaries, and a subset of dynamical capture binaries that form with a sufficiently large periaapse to circularize before merger) have been the predominant focus of the GW community over the past decades [46]. Comparatively, there is a dearth of studies on the detectability of highly-eccentric mergers. In [47] the single burst from a parabolic close encounter was studied, while [6] included the additional signal provided by subsequent bursts. This repeated burst phase was studied in [7] using 2.5 and 3.5 order post-Newtonian (PN) equations-of-motion. It was found that GWs from

this phase may be detectable by Advanced LIGO out to 200–300 Mpc for BH-NS binaries and 300–600 Mpc for BH-BH binaries. Since the PN approximations begin to break down close to merger the evolution was only followed to  $r_p = 10M$ . To model the last stages of merger requires numerical relativity (NR), and there have been a number of numerical studies of eccentric mergers [36–38, 48–53]. However, because of the computational expense of these simulations, it is not possible with current computer resources to follow high-eccentricity binaries through multiple close encounters. The challenge is compounded by a large parameter space including impact parameter, mass ratio, BH spin and NS equation of state. It is thus not reasonable to expect that brute-force numerical simulations will be able to provide templates before the Advanced LIGO era, even accounting for expected increases in computer power.

#### E. Outline of Remainder of Paper

To begin to bridge the gap between large periaapse PN solutions and late-time numerical solutions, we introduce a model for the inspiral, merger, and ringdown of dynamical capture compact binaries. This model is based on geodesic equations of motion in an effective Kerr space-time, combined with quadrupole radiation (Sec. II A) and a version of the Implicit Rotating Source (IRS) model [54, 55] for the merger and ringdown part of the GW signal (Sec. II C). (Except for the IRS extension, and the comparable masses, our hybrid is reminiscent of the “kludge” introduced to study extreme mass ratio inspirals [56–59], based in part on the “semi-relativistic” approach of [60]). We validate this model through a comparison to full numerical simulations in the strong-field regime (Sec. II B) and to the PN approximation for  $r_p > 10M$  (Sec. II D).

The waveforms we produce here are likely not accurate enough for optimal template-based detection of multiple-burst events. However, our waveforms capture the relevant features with sufficient faithfulness that we can use them to assess the efficacy of existing LIGO search strategies. We can also use our waveforms to investigate new search strategies that may be better suited to highly-eccentric mergers. In Sec. III we use this model to evaluate how well these GW signals could be seen with each generation of the LIGO detectors, varying impact parameter (equivalently  $r_p$ ), total mass, and mass ratio. We use various analysis methods: matched filtering with the model templates, filtering with ringdown templates, and a burst search with sine-Gaussian templates. We also estimate how well a hypothetical search using incoherent stacking of bursts following [61] would perform. Though not optimal as matched-filtering, stacking is likely more robust to timing uncertainties in the burst sequence. We find that if capture binaries do exist, in many cases their GW signals will be missed by single burst or ringdown searches (and, as we argue, quasicircu-

lar templates), whereas these sources would be detectable with a full template or a stacked burst search. In particular, GRB051103 [62] had a measured distance of 3.6 Mpc, and no coincident GW signal was found using traditional searches [63, 64]. However, there is a sizable region of the parameter space of dynamical capture binaries that existing searches would have missed. The possibility that the GRB was preceded by an eccentric merger remains a viable possibility.

In Sec. IV we make concluding remarks and comment on the direction of future work.

## II. WAVEFORM MODEL

In this section we describe our model for high-eccentricity merger waveforms. We first look at the inspiral phase in Sec. II A, which can be considered a sequence of GW bursts, each generated at a periaapse passage. In Sec. II B we compare the model expressions we use for the bursts to full numerical simulations. In Sec. II C we discuss the IRS model for the merger and ringdown phase, and in Sec. II D we present examples of the full signal, and make further comparisons to PN results for the inspiral phase.

### A. Repeated Burst Phase

Our objective here is to model the GW signal from an eccentric binary that passes through a series of close encounters prior to merger. To this end, we use a prescription based on the equations of motion of a geodesic in a Kerr spacetime, coupled with the quadrupole formula for gravitational radiation. We identify the mass and total angular momentum of the binary with the mass and spin parameters of the effective Kerr spacetime and the orbital angular momentum and energy with that of the geodesics. This approach has the advantage of reproducing the correct orbital dynamics in the Newtonian limit and general relativistic test particle limit, while still incorporating strong field phenomena such as pericenter precession, frame-dragging and the existence of unstable orbits and related zoom-whirl dynamics. For simplicity, in this first study we restrict attention to equatorial orbits, and for the most part non-spinning BHs (we compare the IRS model to a merger involving a spinning BH in Sec. II C).

The equations for an equatorial geodesic in a Kerr spacetime with mass  $M$  and dimensionless spin  $a$  can be written in first order form using Boyer-Lindquist co-

ordinates as:

$$\begin{aligned}\dot{\tau} &= \frac{\Delta}{\tilde{E}R_0^2 - 2Ma\tilde{L}/r} \equiv Q, \\ \dot{\phi} &= \frac{1}{R_0^2} [\tilde{L}Q + 2Ma/r] \equiv \Omega \\ \dot{r} &= \Delta Q P_r / r^2 \\ \dot{P}_r &= \frac{1}{r^2 Q} [\Omega^2(r^3 - Ma^2) + M(2a\Omega - 1)] \\ &\quad + \frac{P_r^2 Q}{r^3} [a^2 - Mr].\end{aligned}\quad (1)$$

where  $R_0 = r^2 + 2Ma^2/r + a^2$ ,  $\Delta = r^2 - 2Mr + a^2$ ,  $P_r = r^2 \dot{r}/(\Delta Q)$ ,  $\tau$  is proper time, and the overdot indicates a derivative with respect to the coordinate time. Here  $\tilde{E}$  and  $\tilde{L}$  are the energy and angular momentum of the geodesic.

In order to apply these equations to a binary system we go to the center-of-mass frame and let  $\mathbf{r}$  be the separation between the objects. Then we identify the geodesic parameters  $\tilde{E}$  and  $\tilde{L}$  with the reduced energy and angular momentum of the system and promote these quantities to time-dependent variables. To determine the amount of energy and angular momentum radiated away to gravitational waves we use the quadrupole formula:

$$\begin{aligned}\dot{\tilde{E}} &= -\frac{\mu}{5} \ddot{\mathcal{I}}_{ij} \ddot{\mathcal{I}}_{ij} \\ \dot{\tilde{L}} &= -\frac{2\mu}{5} \epsilon^{zij} \ddot{\mathcal{I}}_{ik} \ddot{\mathcal{I}}_{jk}\end{aligned}\quad (2)$$

where  $\mu$  is the reduced mass,  $\mathcal{I}_{ij}$  is the reduced quadrupole moment and  $\ddot{\mathcal{I}}_{ij}$  and  $\ddot{\mathcal{I}}_{ij}$  are written in terms of the variables  $\{r, \phi, P_r, \tilde{E}, \tilde{L}\}$  using (1). We set  $M$  in (1) to the total mass (neglecting orbital energy contributions) and we set  $a = \mu \tilde{L}/M^2 + a_{BH}$ , where  $a_{BH}$  is the net spin of any BHs (though again for this study we focus on non-spinning BHs, where  $a_{BH} = 0$ ). We note that when the orbital angular momentum is large we will have  $a > 1$ . However, this will occur only when the separation  $r$  is also large, so general relativistic effects are small, and no unusual behavior arises from exceeding the Kerr limit. We numerically integrate the coupled set of equations (1) and (2).

The remaining element is to calculate the observed gravitational radiation, which will depend on the intrinsic source parameters (i.e. the mass, mass ratio, eccentricity, and initial periaapse distance), and will also vary with sky location and relative orientation of the source to the detector. At linear order and in the transverse traceless gauge, the complex gravitational wave strain  $h_{\text{opt}}$  a distance  $d$  from an optimally-oriented source is simply related to changes in the quadrupole moment through

$$h^{\text{opt}} \equiv h_+^{\text{opt}} + ih_{\times}^{\text{opt}} \equiv \frac{2}{d} \left( \ddot{\mathcal{I}}_{xx} + i\ddot{\mathcal{I}}_{yx} \right). \quad (3)$$

For general orientations, the emitted strain can be rep-

resented through a mode decomposition as

$$\bar{h} \equiv h_+ + ih_\times = \sum_{\ell=2}^{\infty} \sum_{m=-\ell}^{\ell} h_{\ell m}(t, d) {}_{-2}Y_{\ell m}(\theta, \phi), \quad (4)$$

where  ${}_{-2}Y_{\ell m}$  are the spherical harmonics of spin-weight -2 [65], and  $\theta$  and  $\phi$  being the polar and azimuthal angles of orientation, respectively. For the comparable mass, nonspinning systems that we are primarily interested in, the quadrupole (i.e.  $\ell = 2$ ,  $m = \pm 2$ ) component dominates the strain, so that

$$\bar{h} \approx h_{22}(t, d) {}_{-2}Y_{22}(\theta, \phi) + h_{2-2}(t, d) {}_{-2}Y_{2-2}(\theta, \phi). \quad (5)$$

This completes the approach for calculating the source waveform that reaches a detector. In a later section we will include the sensitivity of the detector in the analysis.

### B. Comparison to fully general-relativistic numerical simulations

To provide some validation for this model we compare several waveforms of single high-eccentricity fly-by encounters from full general-relativistic numerical simulations to those obtained from the geodesic equation with the quadrupole formula. The simulations include a 4:1 mass ratio BH-NS system [37], an equal mass NS-NS system [38], and an equal mass BH-BH system. The NR simulations were all performed using the code described in [66].

In Fig. 1 we show several such examples from NR simulations of the 4:1 BH-NS system alongside corresponding waveforms from our model with best-fit parameters. The peak amplitude of the geodesic is scaled to be the same as in the simulations. The fit is performed by finding the initial orbital parameters that maximize the phase overlap between the waveforms (see e.g. [67]). In this regime the match between the waveforms is most sensitive to  $r_p$  as opposed to  $e$ . As can be seen, the fly-by waveforms from our model provide a good match to those from simulations. Even close to the effective innermost stable orbit (ISO) for the BH-NS system (the bottom panels of Fig. 1), where the system begins to show evidence of whirling behavior, our model is able to approximately capture the shape of the waveform.

In Table I we give the fit parameters, amplitude enhancement, and overlap. We also show the approximate initial orbital parameters ( $r_p$  and  $e$ ) of the simulation obtained by equating a Newtonian estimate of the reduced orbital energy and angular momentum at the beginning of the simulation with the  $\tilde{E}$  and  $\tilde{L}$  parameters of the geodesic model described above. (Note, this is different from the *Newtonian* values for  $r_p$  and  $e$  used in [37, 38].) For most of the BH-NS systems in Table I we can see that the enhancement required to match the amplitude of our model to the simulation results is  $\sim 4 - 11\%$ . This is presumably due to aspects not captured by this

Binary	Sim. <sup>a</sup>		Fit <sup>b</sup>		$A^c$	Overlap <sup>d</sup>
	$r_p$	$e$	$r_p$	$e$		
NS-BH	8.30	1.00	8.77	1.00	1.04	0.99
NS-BH	8.00	0.80	7.97	0.81	1.11	0.98
NS-BH	5.62	1.00	5.61	1.00	1.11	0.97
NS-BH	5.04	1.00	4.26	1.00	0.61	0.74
BH-BH	8.71	1.00	8.23	1.00	1.16	0.99
NS-NS	8.71	1.00	7.82	1.00	1.28	0.96

TABLE I: Fit parameters for close-encounter GWs

<sup>a</sup> Approximate initial parameters of the geodesic model based on the initial orbital energy and angular momentum of the simulation.

<sup>b</sup> Initial parameters of the geodesic model that best fit the simulation data.

<sup>c</sup> Amplitude enhancement applied to waveform from best fit geodesic model.

<sup>d</sup> Overlap between simulation and best fit geodesic model.

simple model, such as finite-size effects, as well as truncation error from the simulations. The one case where the amplitude of the simulation waveform was below the model result was a simulation with strong whirling behavior (bottom-right panel of Fig. 1) where the NS had large  $f$ -mode oscillations excited as described in [37].

We also compare the geodesic model with an equal mass BH-BH and an equal mass NS-NS system as shown in Fig. 2. Although one would expect a geodesic approximation to be most accurate in the limit that one mass is much larger than the other, it still provides good fits for equal masses. This model, however, does not attempt to include finite-size effects (such as the  $f$ -mode excitation visible in the later part of the bottom of Fig. 2), which would be required to address questions related to measuring the NS equation of state from such GW signals.

### C. Merger model

After a binary has evolved through some number of close-encounters, it will merge. In order to include the waveforms resulting from merger, we supplement the model outlined in Sec. II A with a version of the Implicit Rotating Source (IRS) model [54, 55] for the merger and ringdown part of the GW signal. Note that the IRS assumes the waveform is circularly polarized. This is not strictly valid for the complete merger/ringdown phase of eccentric binaries, though as we show below, it does provide a reasonably good approximation to results from numerical simulations. As with other aspects of our waveform model, this assumption could be refined in the future, but it is adequate for the purpose of testing the efficacy of existing search strategies for detecting eccentric binaries.

In particular, we model the phase evolution to asymptotically approach the least damped quasinormal mode

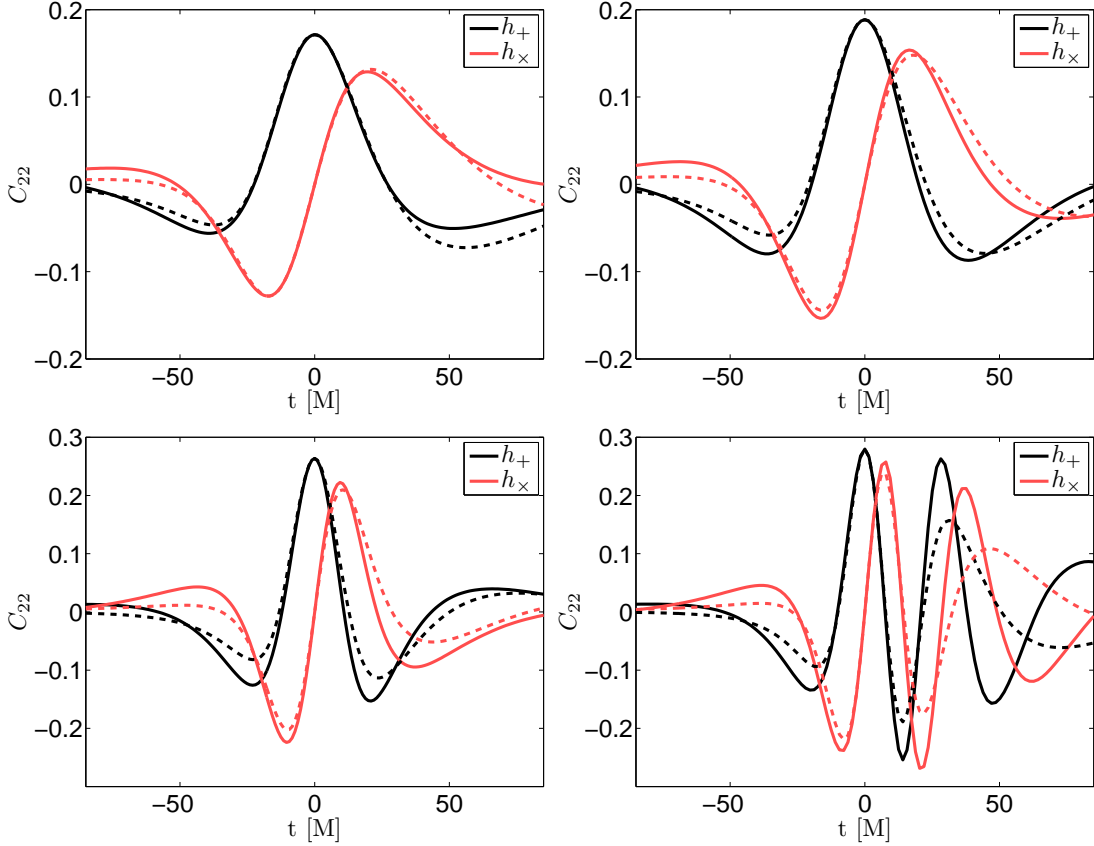


FIG. 1: Comparison of the  $\ell = 2$ ,  $m = 2$  component of  $\bar{h}$  for fly-by waveforms from 4:1 BH-NS simulations (solid) and our model with best-fit periapse distance (dashed). The approximate effective geodesic orbital parameters of the simulated system (left to right, top to bottom) are:  $(r_p, e) = (8.3, 1.0)$ ,  $(8.0, 0.8)$ ,  $(5.6, 1.0)$ , and  $(5.0, 1.0)$ . The fit parameters are given in Table I.

frequency of the final BH,  $\omega_{\text{QNM}}$ , via

$$\omega(t) = \omega_{\text{QNM}}(1 - \hat{f}) \quad (6)$$

where

$$\hat{f} = \frac{c}{2} \left(1 + \frac{1}{\kappa}\right)^{1+\kappa} \left(1 - \left(1 + \frac{1}{\kappa} e^{-2t/b}\right)^{-\kappa}\right). \quad (7)$$

Here  $b = 2Q/\omega_{\text{QNM}}$  is determined by the quality factor and frequency of the final BH, and  $\kappa$  and  $c$  are free parameters of the model. The amplitude is given, up to an overall factor  $A_0$ , by

$$A = \frac{A_0}{\omega(t)} \left( \frac{|\dot{\hat{f}}|}{1 + \alpha(\hat{f}^2 - \hat{f}^4)} \right)^{1/2} \quad (8)$$

where  $\dot{\hat{f}} = d\hat{f}/dt$ , and  $\alpha$  is a free parameter. We find that  $\alpha = 72.3/Q^2$  provides a reasonably good fit to our numerical simulations.

In Fig. 3 we show a comparison between simulation results of BH-NS mergers and the best match IRS model waveforms where we let  $\kappa$  and  $c$  be fitting parameters. In Fig. 4 we show the same thing for equal mass NS-NS

and BH-BH mergers. This simple model will not capture disruption or other matter effects, and best-fit values for  $\kappa$  and  $c$  will have some dependence on the parameters of the binary, such as the impact parameter preceding merger. However, when studying signal detectability we fix  $\kappa = 0.64$  and  $c = 0.26$ , which empirically provides reasonably good fits to a large number of simulated waveforms, and therefore provides an adequate representation of a generic eccentric merger. We attach the IRS part of the waveform to the model from Sec. II A when the separation reaches the light ring of the effective Kerr space-time.

#### D. Model Properties and Comparison to Post-Newtonian

Combining the inspiral and merger models allows us to generate complete waveforms for dynamical capture binaries. In Fig. 5 we show one such example for a 4:1 mass ratio system with initial orbital parameters corresponding to  $r_p = 8M$  and  $e = 1$ . The waveform shows the decreasing time interval between bursts from close encounters as  $r_p$  and  $e$  decrease due to gravitational radi-

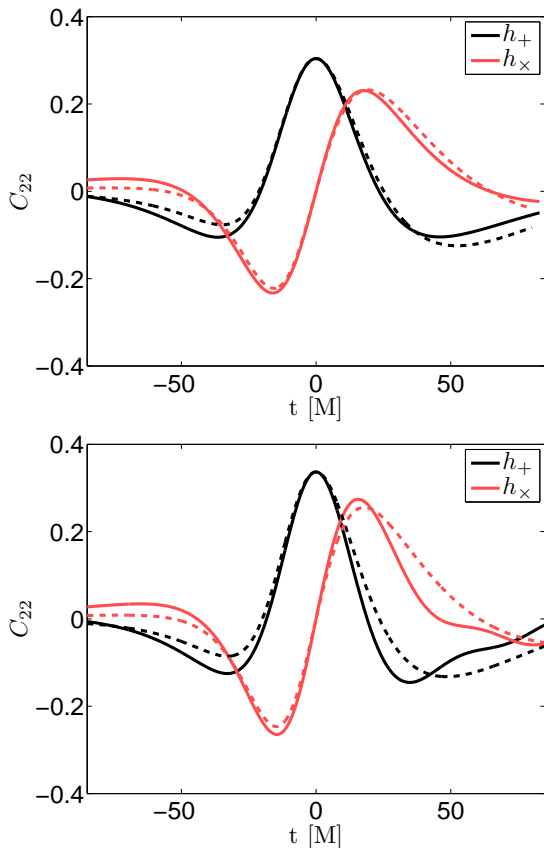


FIG. 2: Comparison of the  $\ell = 2$ ,  $m = 2$  component of  $\bar{h}$  for fly-by waveforms from equal mass BH-BH (top) and NS-NS (bottom) simulations (solid lines) and our model (dotted lines) with best-fit parameters. The approximate effective geodesic orbital parameters of the simulated systems are  $(r_p, e) = (8.7, 1.0)$  for both cases. The fit parameters are given in Table I. The feature in the waveform after the peak in the NS-NS simulation is from  $f$ -mode excitation that occurs during the close encounter.

ation. The number and timing of the bursts is a sensitive function of the amount of energy and angular momentum radiated in each close encounter. In Fig. 6 we show how  $r_p$  and  $e$  evolve according to this model for some example binaries. It can be seen that the binaries considered here, which begin on parabolic orbits with  $r_p \leq 10 M$ , still have non-negligible eccentricity all the way to merger.

We can also compare this model to that given by the 2.5 and 3.5 order PN approximation as used in [7]. In Fig. 7 we show how the difference in the energy and angular momentum radiated away in a close encounter for 2.5 or 3.5 PN relative to our model changes with initial impact parameter. The geodesic model predicts less energy and momentum loss than 2.5 PN but more than the 3.5 PN. At large impact parameters the three different models converge. At smaller impact parameters the 2.5 and 3.5 PN approximations begin to diverge. As shown in [68], the PN approximation fails to converge (or even to provide physically sensible results in the case of 3.5

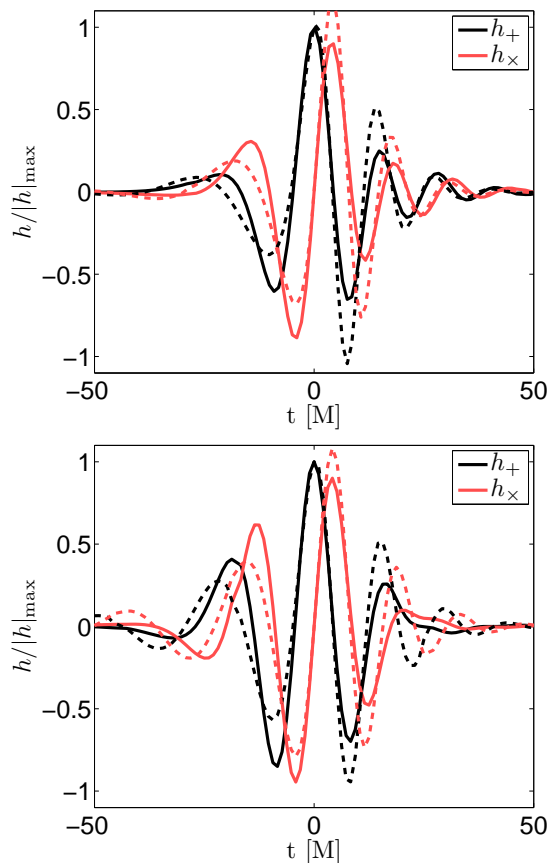


FIG. 3: Comparison of the merger GW strain from a 4:1 BH-NS simulation (solid lines) and the IRS model (dotted lines) with best fit parameters. The top panel shows a case where the initial BH was non-spinning. The bottom panel shows a case with  $a_{\text{BH}} = 0.5$ , which results in more whirling behavior and tidal-disruption of the NS. The best fit parameters in (7) are  $(\kappa, c) = (0.66, 0.28)$  (top) and  $(0.46, 0.18)$  (bottom), and the matches are 0.98 and 0.96 respectively. The match is weighted based on the “whitened” waveforms as described in Sec. III assuming a total mass of  $10 M_\odot$ .

PN) for  $r_p \lesssim 10 M$ .

### III. DETECTABILITY

#### A. Detector Modeling

Having developed a model for the gravitational waveforms emitted by high-eccentricity binaries, we can now assess the detectability of these signals for different source parameters and detectors. The measured strain  $h$  is given by

$$h = \Re[F\bar{h}] = F_+ h_+ + F_\times h_\times, \quad (9)$$

where  $F \equiv F_+ - iF_\times$  is the sky-dependent detector response. The signal-to-noise ratio (SNR)  $\rho$  using a per-

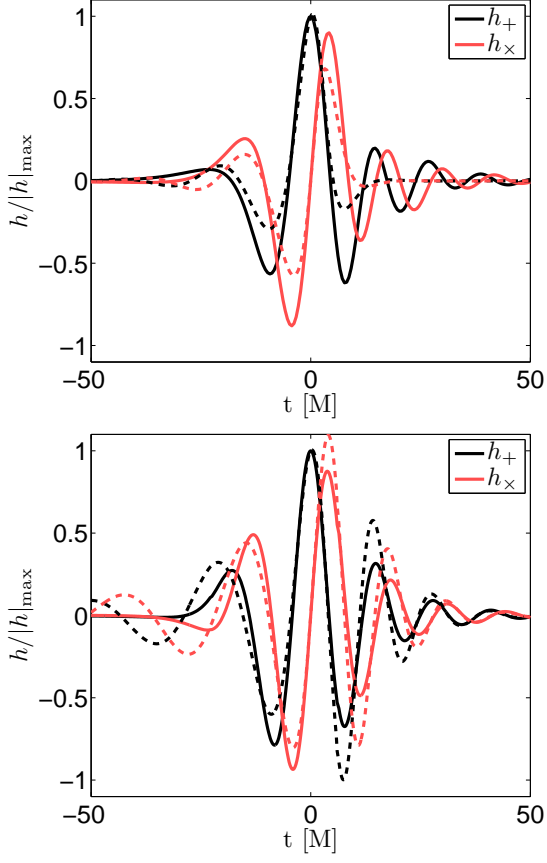


FIG. 4: Comparison of merger waveforms from an equal mass BH-BH simulation (top) and NS-NS simulation that forms a BH (bottom) with the IRS model (dotted lines) with best fit parameters. The best fit parameters in (7) are  $(\kappa, c) = (0.31, 0.03)$  (top) and  $(0.36, 0.19)$  (bottom), and the matches are 0.98 and 0.97 respectively. The match is weighted based on the “whitened” waveforms as described in Sec. III assuming a total mass of  $20 M_\odot$  and  $2.8 M_\odot$  for the BH-BH and NS-NS binaries, respectively.

fectly matched filter is given by

$$\rho^2 = \langle h|h \rangle, \quad (10)$$

where  $\langle \cdot | \cdot \rangle$  denotes a noise-weighted inner product given by

$$\langle h_1 | h_2 \rangle \equiv 2 \int_0^\infty df \frac{\tilde{h}_1^* \tilde{h}_2 + \tilde{h}_1 \tilde{h}_2^*}{S_n}, \quad (11)$$

where  $S_n(f)$  is the power spectral density of the detector noise, and  $\tilde{h}$  denotes the Fourier transform of the original  $h$  time series. Because we limit our model to the quadrupole component of the signal, and we focus on detectors (like LIGO) for which the gravitational wavelength is much longer than the detector’s armlength, we can trivially relate the SNR of an optimally oriented and located source to the SNR of an orientation- and

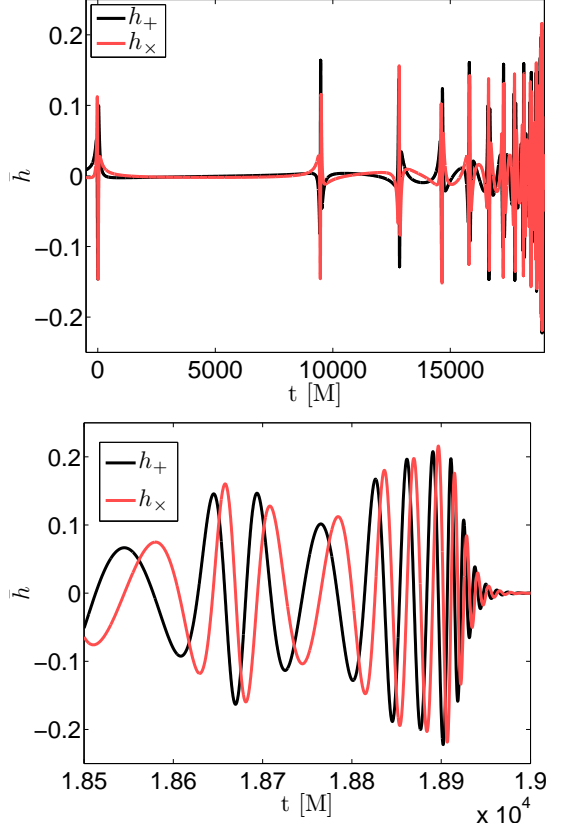


FIG. 5: GW strain generated with our model and initial conditions  $r_p = 8M$  and  $e = 1$ . The top panel shows the entire waveform while the bottom panel shows a zoomed-in view of the end of the waveform.

sky-location-averaged source. For such detectors, the response function to the two waveform polarizations,  $F_+$  and  $F_\times$ , is simply the root-mean-squared (rms) average over the sky location and polarization angles  $\sqrt{\langle F_{+, \times}^2 \rangle} = \sqrt{1/5}$  [69]. Likewise, the rms average over source orientations is  $\sqrt{\langle -2Y_{2, \pm 2} \rangle} = \sqrt{1/5}$ , so that  $\sqrt{\langle \rho^2 \rangle} = \rho_{\text{opt}}/5$ . We can further define the characteristic strain  $h_c$  for both a signal and detector noise. Given Eq. (11) and the typical practice of plotting sensitivity curves logarithmically, it is useful to define  $h_c \equiv \sqrt{\langle -2Y_{2, \pm 2} \rangle} f \tilde{h}_{\text{opt}}$  for signals and  $h_c \equiv \sqrt{f S_n / \langle F^2 \rangle}$  for detector noise, so that both signal and noise are characterized as a dimensionless strain, and the ratio of signal- $h_c$  to noise- $h_c$  is the square root of the integrand for  $\rho^2$  when integrated over logarithmic frequency intervals  $df/f$ . We show this characterization of signal and noise in Fig. 8.

For assessing the relative contribution of different waveform segments to the SNR, it is often convenient to work in the time domain by constructing “whitened” waveforms [70], which weight the amplitude of the waveform as a function of frequency to account for the pres-



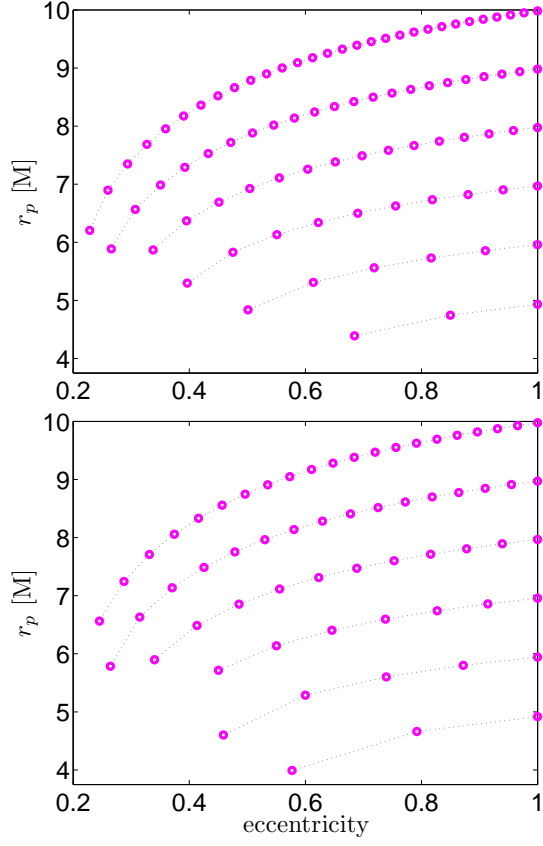


FIG. 6: Evolution of orbital parameters for a 4:1 (top) and an equal mass ratio (bottom) binary. The effective eccentricity is calculated from successive apoapse and periape distances as  $e = (r_a - r_p)/(r_a + r_p)$ .

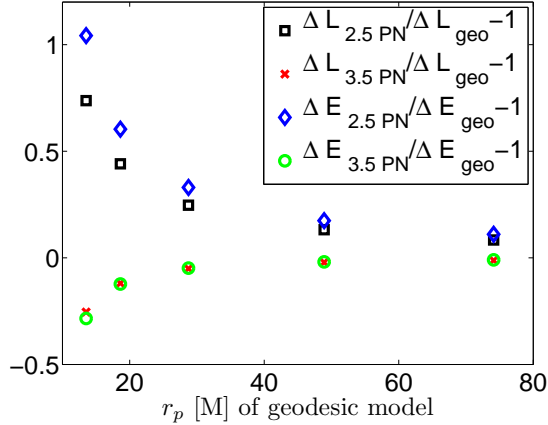


FIG. 7: Relative difference in energy and angular momentum lost in a close encounter for the 2.5 and 3.5 PN approximation versus our model. For this comparison the orbits are chosen to initially have zero energy and the same value of angular momentum which, for a geodesic with the same initial conditions, corresponds to the value of  $r_p$  indicated on the  $x$ -axis.

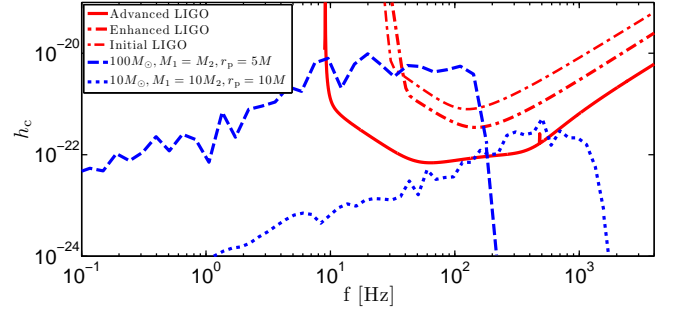


FIG. 8: The characteristic strain  $h_c$  is shown for the initial (thin dash-dotted), Enhanced (dashed), and Advanced LIGO (solid) detectors, as well as for two example signals at  $D_L = 1$  Gpc. The first signal corresponds to an orientation-averaged source with  $M = 100 M_\odot$ ,  $q = 1$ , and  $r_p = 5M$  (dashed), and the second signal is from a source with  $M = 10 M_\odot$ ,  $q = 0.1$ , and  $r_p = 10M$  (dotted). Both signal spectra are smoothed to diminish fluctuations and make the trend more clear. The system with  $q = 0.1$  has little contribution from the merger, so the repeated burst phase dominates the spectra, with  $h_c \propto f$ , whereas the  $q = 1$  system signal comes largely from the merger, where  $h_c \approx \text{constant}$  over a small band of frequencies.

ence of noise in the detector,

$$h' = \int_{-\infty}^{+\infty} df \frac{\tilde{h}}{\sqrt{S_n}} e^{-i2\pi ft}. \quad (12)$$

With these whitened vectors, the noise-weighted inner product (11) can be re-expressed in the time domain:

$$\langle h_1 | h_2 \rangle \equiv \int_{-\infty}^{\infty} dt h_1^*(t) h_2'(t). \quad (13)$$

Figure 9 shows portions of the whitened waveform for two example cases with the same mass ratio and initial  $r_p$  and  $e$ , but different masses. The upper panel shows the burst with the largest SNR contribution for a source with total mass  $M = 10 M_\odot$ , while the lower panel shows the loudest burst for  $M = 100 M_\odot$ . The different masses change the frequency of the signal, so different bursts are emphasized by the detector sensitivity; in particular, for larger masses the final burst and merger are emphasized. We also show best-fits for two types of templates that are described below.

## B. Templates and detection strategies

While quasicircular sources are searched for using matched-filtering, eccentric systems are far more susceptible to modeling error in the relative timing and phase of signal bursts, which is why we focus our attention on alternative approaches to detection. For example, a

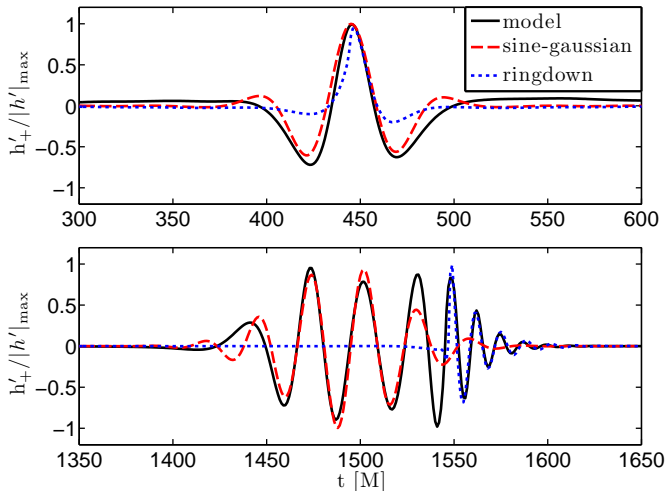


FIG. 9: Whitened waveforms for a  $10 M_\odot$  (top) and a  $100 M_\odot$  (bottom) binary with initial  $e = 1$  and  $r_p = 5M$ , along with the (whitened) best fit template among sine-Gaussian and ringdown templates.

small modeling error in the energy lost during a particular periaapse passage  $\delta E$  will induce a timing error in the arrival time of the subsequent burst  $\delta T$  given by  $\delta T \propto \delta E(1 - e)^{-5/2}$ . Therefore, dynamical capture binaries are far more challenging to model with sufficient accuracy to apply matched filtering due to their large eccentricities.

We assess detection prospects of GWs from capture binaries for two currently used templates, sine-Gaussian (SG) and ringdown (RD) templates, as well as an idealization of a third strategy based on combining an excess power search with stacking. The SG and RD both take the form

$$\bar{h} = A \exp \left[ - \left( \frac{t - t_o}{\tau} \right)^\gamma + i\omega(t - t_o) - i\phi_o \right], \quad (14)$$

where  $\gamma = 1$  and  $t \geq t_o$  for the RD templates, and  $\gamma = 2$  with  $-\infty < t < \infty$  for the SG templates. Here  $A$  is the overall amplitude,  $t_o$  and  $\phi_o$  are the time and phase of the template's amplitude peak,  $\tau$  sets the e-folding of the amplitude, and  $\omega$  is the constant frequency.

In addition to assessing the performance of two burst templates, we calculate a rough approximation of the potential performance for an excess power search that accumulates power from the entire signal [61], which we will call a power-stacking search. Here, the data would be transformed to a time-frequency (TF) tiling using a basis suitable to capturing individual bursts within a tile, and then power from different tiles corresponding to bursts, as informed by our model, is combined. Whereas in most existing TF searches an individual element must have enough power to exceed some threshold, with that threshold being large enough to avoid many false alarms, the approach we describe does not require that the signal be detectable in any single TF element.

In the case of a monochromatic signal, the SNR from optimal filtering will accumulate with the number of cycles  $N$  as  $\sqrt{N}$ , while the excess power in stacking TF elements (constructed using any basis) overlapping the given frequency will accumulate as  $N^{1/4}$ . The signals from high-eccentricity binaries are not monochromatic, but given the typically large number of bursts occurring in-band, and the relative flatness of both the source spectrum and the detector sensitivity across its most sensitive band, we expect the aforementioned scalings to hold approximately for realistic signals.

This search would be very similar to the stacked search proposed for combining potential GW counterparts to observed electromagnetic signals from soft gamma repeaters [61]. There, TF elements were aligned in time based on the observed bursts, and they demonstrated the  $N^{1/4}$  SNR scaling when adding power for identical injected signals. Since we do not have a separate observational trigger, our proposed search would sum power along elements overlapping bursts as indicated by our waveform model. We leave it to future work to fully investigate this, though here we assume we can achieve the  $N^{1/4}$  SNR scaling, and thus can estimate the performance of a power-stacking search by noting that optimal filtering should outperform power stacking by  $N^{1/4}$ . Hence, we can approximate the effective excess power SNR as  $\rho_{EP} \approx N^{-1/4} \rho$ . This simple estimate will constitute our third search technique in our subsequent analysis.

We do not employ quasicircular (QC) templates, although they have thus far been the only tool employed to search for long-lived signals. QC templates will generically fail to match the performance of any of the above methods for the repeated burst phase of eccentric sources for the following reasons. First, during the long intervals between eccentric bursts a QC template will still be integrating power from the data, which is predominantly noise. Specifically, the ratio of the characteristic timescale of an eccentric burst to the period between bursts is roughly

$$\frac{\tau_{\text{GW}}}{T} \approx (1 - e)^{3/2}. \quad (15)$$

In other words, there will be  $\sim (1 - e)^{-3/2}$  additional cycles between bursts in a QC signal with the same periaapse. More over, even if the QC template is phase-aligned to a particular burst, since the time between bursts is much larger than the GW period, the rest of the template will effectively have random phase alignment with other bursts in the sequence, and on average no additional SNR will be acquired. To summarize, typically the best matched QC template will only integrate signal about the loudest burst, but even so the performance will not be as good as a single burst search due to the larger integrated noise accumulated over the period of the QC template (expect for the higher mass systems where only the final merger/ringdown signal is in band).

### C. Results

We calculate two useful quantities related to the SNR: the detectability horizon and the detection probability. Since  $h \propto D_L^{-1}$ , where  $D_L$  is the luminosity distance, we can use (10) to calculate the distance (which we call the detection horizon) at which a sky- and orientation-averaged source could be observed with an SNR of 8 using optimal filtering. The detection probability for a given strategy is simply the ratio of the volume in which the strategy could detect a source with some SNR to the volume in which the source could be seen with the same SNR using optimal filtering. In the remainder of this section, we will calculate these quantities for various cases of interest. We consider the following configurations:

- three detector sensitivities, corresponding to initial, Enhanced, and Advanced LIGO;
- three detection strategies, including SGs, RDs, and power stacking, and how they compare to optimal filtering;
- three intrinsic system parameters:
  - total system mass  $M$ , ranging from  $1\text{ M}_\odot$ – $2000\text{ M}_\odot$ ;
  - mass ratio  $q$  of the binary components, ranging from  $0.01$ – $1$ ;
  - initial  $r_p$ , ranging from  $5M$ – $10M$  (with initial  $e = 1$ ; we exclude  $r_p < 5M$  simply because in most cases it is a directly collision qualitatively similar to  $r_p = 5$ , and see [7] for a study of  $r_p > 10M$ ).

In Fig. 10, we show contours of constant horizon distance as a function of  $q$  and  $r_p$  for initial LIGO, assuming optimal filtering, SG templates, and power stacking. Two contours of note, at  $0.77$  and  $3.6$  Mpc, correspond to the distances of GRB070201 [71] and GRB051103 [62], respectively. These were two nearby gamma-ray bursts observed by Swift during the S5 initial LIGO run, while two interferometers were actively collecting data at or near initial LIGO’s design sensitivity. However, no signal was found in the LIGO data using the methods applied (specifically, various burst and quasicircular inspiral templates) for these GRBs, nor for any of the 137 GRBs (35 with measured redshifts) that occurred while initial LIGO was taking science data during its S5 run at or near design sensitivity [63, 64]. Thus in Fig. 10 we restrict the mass ratio to the range  $0.1$ – $1$ , with one of the masses fixed at  $1.35\text{ M}_\odot$ , to focus on systems including a neutron star that are expected to generate GRBs. In the case of a dynamical capture binary source at  $0.77$  Mpc, the signal is sufficiently loud that even suboptimal searches like SG templates would detect them. However, for a source at  $3.6$  Mpc, whereas an optimal filter would have detected a signal from a large region of the parameter space, including all cases with  $q < 0.5$  or  $r_p > 7.5\text{ M}$ ,

and power stacking would recover signals with  $q < 0.4$ , SG templates are far less effective, and would only recover a small sliver of parameter space with  $q < 0.2$ . This suggests the possibility that the searches applied to the LIGO data would not have found the gravitational wave counterpart to GRB051103 if it was in the form of a dynamical capture binary. Furthermore, across the full parameter space explored, the difference in performance among these three searches is substantial, with optimal filtering detecting sources as far as  $D_L = 50$ – $100$  Mpc, while power stacking only reaches  $D_L \approx 30$  Mpc, and SG templates only reach  $D_L \approx 15$  Mpc.

Figures 11 and 12 show, for Enhanced and Advanced LIGO respectively, contours of detection horizon as a function of mass and mass ratio at a fixed  $r_p = 6M$  using an optimal filter and SG and RD templates. The primary difference in both cases is the degradation of performance for higher mass ratios (smaller  $q$ ), with the SG performing as well as or better than the RD templates across much of the parameter space, with the exception of comparable mass ratios, where the ringdown signal is most emphasized. For each search, Enhanced LIGO could detect an equal mass binary with  $M = 100\text{ M}_\odot$  out to  $D_L = 1$  Gpc, and Advanced LIGO will see the same sources beyond  $10$  Gpc.

The relative performance of SG and RD is further demonstrated in Figs. 13 and 14, which show the detection probabilities of each template (equivalently, the ratio of the detectable volume using the templates to the volume using optimal filtering). SG templates perform best for  $M \approx 200\text{ M}_\odot$  systems using Enhanced LIGO and  $M \approx 1000\text{ M}_\odot$  systems using Advanced LIGO, largely independent of the mass ratio. Interestingly, RD templates perform best for comparable mass binaries regardless of total mass for Enhanced LIGO, whereas no such clear general behavior is observed for Advanced LIGO. This can be understood because Enhanced LIGO always has fewer cycles in band than Advanced LIGO, so that the merger-ringdown constitutes a larger fraction of the total SNR, with that fraction further enhanced for comparable masses (since  $\rho \propto \eta = m_1 m_2 / M^2$  for inspirals, but  $\rho \propto \sqrt{\eta}$  for ringdowns [72]). Advanced LIGO shows no such behavior because the number of inspiral cycles is so large that the merger-ringdown rarely dominates the total SNR.

Figures 15 and 16 again show contours of horizon distance for Enhanced and Advanced LIGO, but as a function of total mass and initial pericenter distance at fixed  $q = 1$ . Both  $q$  and  $M$  rather strongly affect the detectability of sources over the range of masses considered.  $r_p$  moderately affects detectability for lower mass systems ( $M \lesssim 20\text{ M}_\odot$ ), though very little for higher mass systems (which is expected since the number of bursts varies significantly with  $r_p$  in the range  $5M < r_p < 10M$ , but as the mass increases fewer of the initial bursts are in band). SG templates outperform RD templates for all but the extremely high-mass systems, and a small region of extremely-low mass systems with very small  $r_p$ , that

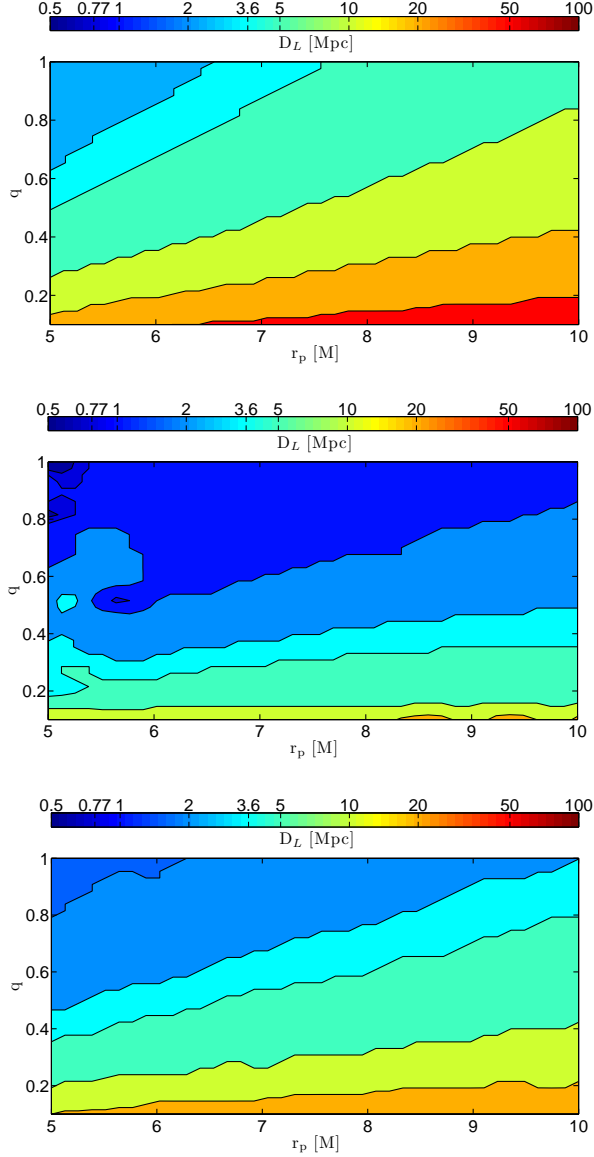


FIG. 10: Contours of horizon distance ( $\rho = 8$ ) as a function of mass ratio  $q$  and pericenter separation  $r_p$  for initial LIGO using an optimal filter (top), sine-Gaussian templates (middle), and an estimate of a power-stacking search (bottom) as described in the text. We fix one component to be a  $1.35 M_\odot$  neutron star and change the total mass with mass ratio accordingly. We include a contour at  $D_L = 0.77$  Mpc and another at  $3.6$  Mpc, to show the region of parameter space where existing LIGO searches would not have seen a gravitational-wave counterpart to GRB070201 [71] and GRB051103 [62], respectively.

merge after  $\mathcal{O}(1)$  orbit. This is also clear in Figs. 17 and 18, which shows corresponding detection probabilities. In addition to SG and RD templates, Figs. 16 and 18 show the relative performance of a stacked power search, which readily outperforms burst template searches for the full range of parameters. Since this is the case for  $q = 1$ , it

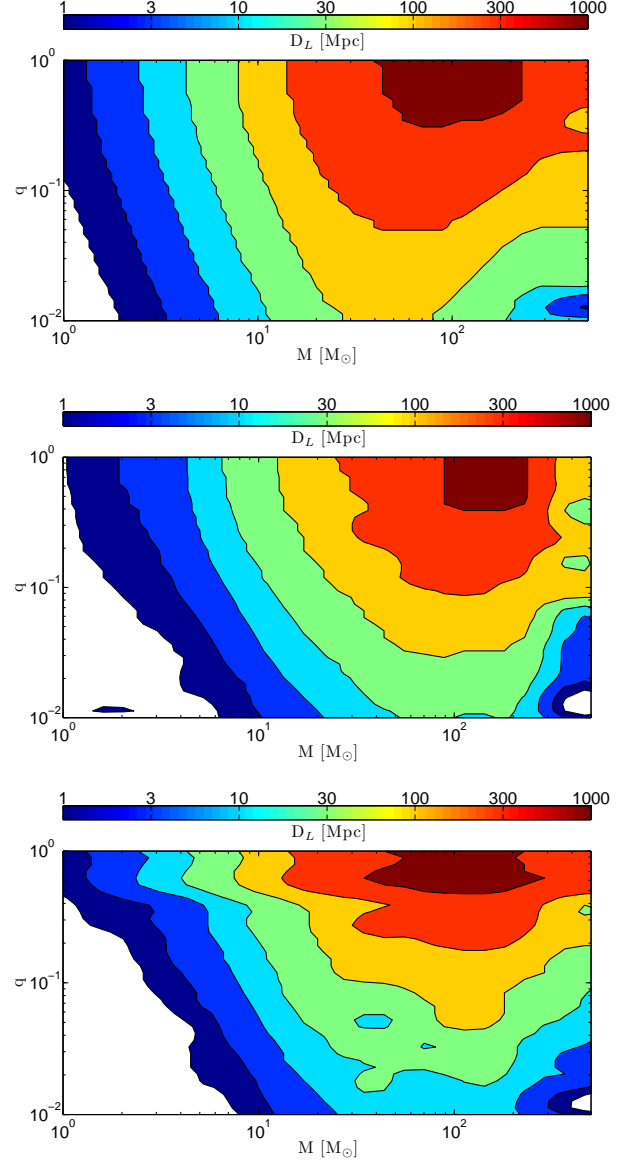


FIG. 11: Contours of horizon distance as a function of rest mass  $M$  and mass ratio  $q$  for Enhanced LIGO using an optimal filter (top), sine-Gaussian templates (middle), and ring-down templates (bottom) for an initial pericenter separation of  $r_p = 6M$ .

will apply more so for cases with  $q < 1$ , as they experience more cycles, so that we can conclude that a power stacking search will always outperform a burst search, and is likely to be the optimal search approach in the absence of a matched-filter bank. SG and RD templates perform best for  $M$  in the range  $100 M_\odot$ – $200 M_\odot$  for both Enhanced and Advanced LIGO, with the range of horizon distances being the same as in the  $M - q$  plots. This is as expected given that setting  $q = 1$  maximizes the signal power at fixed  $M$  and  $r_p$ .

As shown in Fig. 18, all three search methods approach optimal-filter performance for large masses  $M \gtrsim 500 M_\odot$ ,

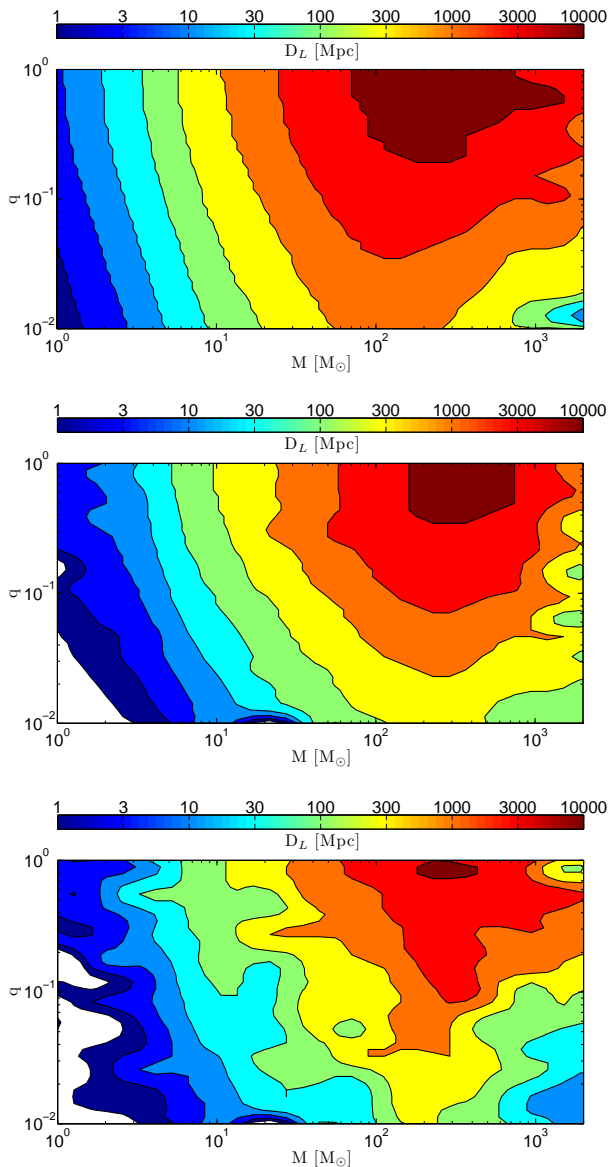


FIG. 12: Contours of horizon distance as a function of rest mass  $M$  and mass ratio  $q$  for Advanced LIGO using an optimal filter (top), sine-Gaussian templates (middle), and ringdown templates (bottom) for an initial pericenter separation of  $r_p = 6M$ .

since all three methods benefit from having the SNR concentrated in a small number of cycles. However, for lower masses and therefore a larger number of in-band cycles, the SG and RD template performances degrade much more rapidly than power stacking. Whereas SG and RD templates reach detection probabilities as low as 0.01%, power stacking remains above 10% for the full parameter space considered. Since our power-stacking estimate is an idealization, uncertainties in the timing and frequencies of eccentric bursts may degrade the performance of a true TF power-stacked search. On the other hand the results of [61] suggest this method is rather robust to tim-

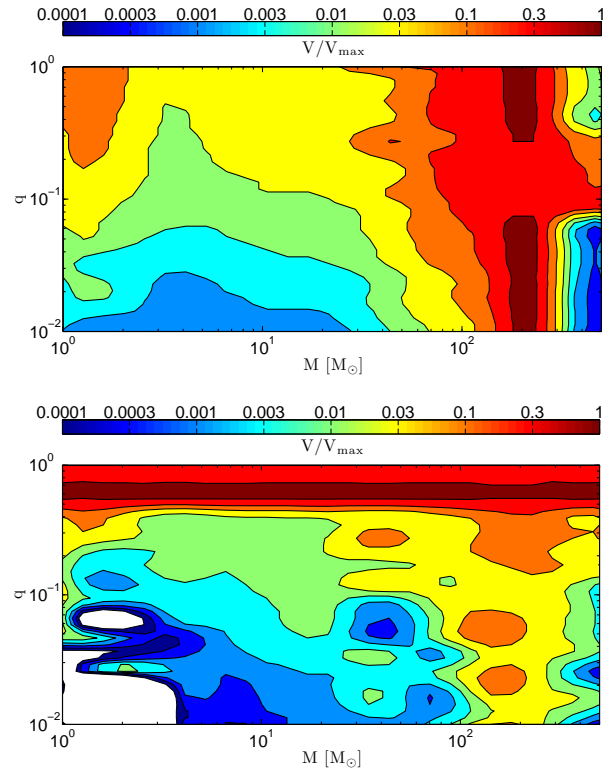


FIG. 13: Contours of detection probability  $p \equiv V/V_{\max}$  as a function of rest mass  $M$  and mass ratio  $q$  for Enhanced LIGO for a source inside the optimal filtering distance horizon, using sine-Gaussian (top) and ringdown (bottom) templates for an initial pericenter separation of  $r_p = 6M$ .

ing uncertainties that are smaller than the characteristic time of each burst .

#### IV. CONCLUSIONS

We have developed a novel waveform model for eccentric binary gravitational waveforms which can be applied for  $r_p \leq 10M$ , where conventional post-Newtonian waveforms fail. Such binaries may form through dynamical capture in dense stellar environments. Our model is not sufficiently accurate to generate a matched-filter bank, and doing so will be very challenging for large eccentricities. However, the model is adequate to supply mock signals to explore the performance of existing LIGO searches in detecting highly-eccentric binary systems. Of existing search strategies, the ringdown and burst searches are best adapted to these systems. However, we find that a large fraction of the parameter space, where we included impact parameter  $5 \leq r_p \leq 10M$  (see [7] for a complimentary study of  $r_p \geq 10M$ ), total mass  $M \in [1, 2000] M_\odot$  and mass ratio  $q \in [0.01, 1]$ , has a significantly smaller horizon distance than what is in principle achievable with a matched filter search. This implies a corresponding volume of sources could have been missed

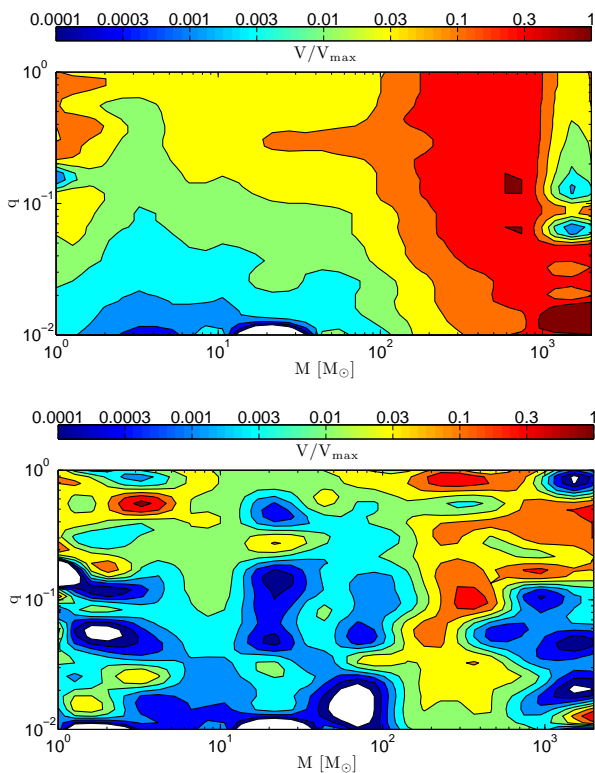


FIG. 14: Contours of detection probability  $p \equiv V/V_{\max}$  as a function of rest mass  $M$  and mass ratio  $q$  for Advanced LIGO for a source inside the optimal filtering distance horizon, using sine-Gaussian (top) and ringdown (bottom) templates for an initial pericenter separation of  $r_p = 6M$ .

in prior searches and may be missed in future searches if better adapted strategies are not employed.

Though it may be impractical to construct templates in the near future (via numerical or analytical methods) for these systems that are accurate enough for optimal searches, a refinement of the waveform model presented here should be adequate for informing a power-stacking search. This method has the potential to increase SNR by  $\approx N^{1/4}$  for an  $N$ -burst event compared to a single burst search. Though less than the effective  $N^{1/2}$  scaling of a full template search, this would still be a significant improvement. Note also that even for systems with larger impact parameters that do evolve to an essentially quasicircular inspiral following the burst phase, for most expected binary parameters the burst phase will be within the band of ground-based detectors. Thus, the quasicircular inspiral phase will be truncated compared to a primordial quasicircular inspiral, and though such a system may still be detectable with a quasicircular template, it would of course be mis-identified, and a bias would be introduced in the estimation of the binary parameters.

For future work, we intend to implement a power-stack search using this waveform model to fully explore the efficacy of this method and its (in)sensitivity to timing errors, as well as continue to refine the model to include

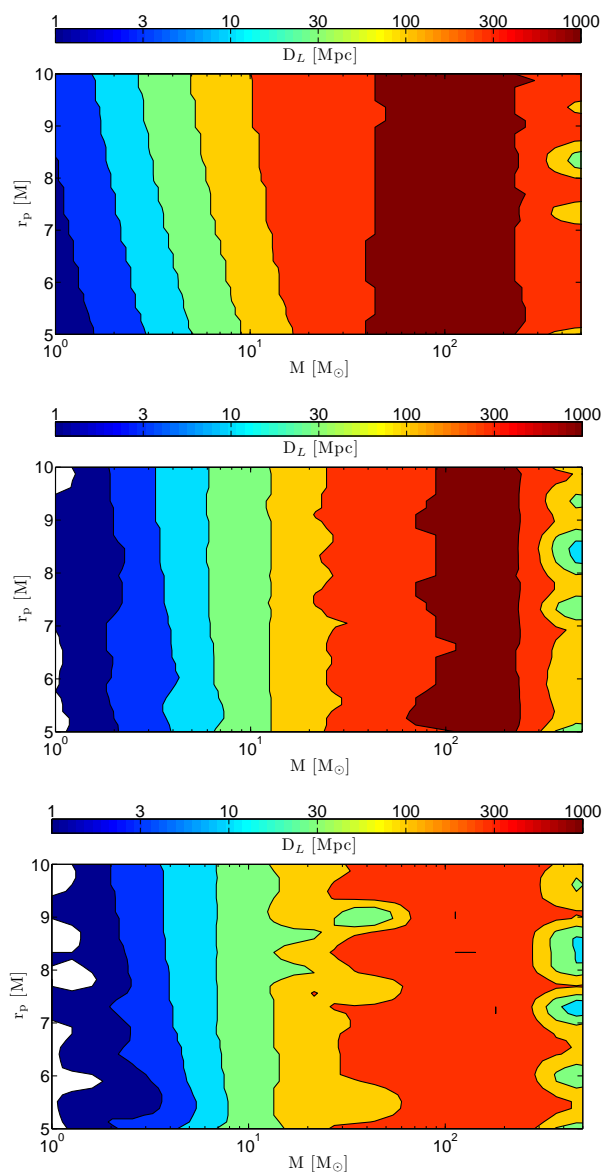


FIG. 15: Contours of horizon distance as a function of rest mass  $M$  and pericenter separation  $r_p$  for Enhanced LIGO using an optimal filter (top), sine-Gaussian templates (middle), and ringdown templates (bottom). The mass ratio is  $q = 1$ .

(for example) spin precession and finite body effects for neutron stars. We mentioned that the standard PN equations are ill-suited to studying the late stages of mergers, in particular for high eccentricity binaries, motivating our development of the effective Kerr with radiation-reaction model described here. However, the Effective One Body (EOB) approach [73] is an alternative to the PN expansion that is well behaved all the way to merger for quasicircular orbits. This approach has recently been extended to generic orbits [74], and it will be interesting to explore EOB as the basis for a repeated burst waveform model.

### Acknowledgments

We would like to thank the participants of the KITP “Rattle and Shine” conference (July 2012) for useful discussions. This research was supported by NSF grants PHY-0745779 (FP) and AST-0908365 (JL), the Alfred P. Sloan Foundation (FP) the Simons Foundation (FP), and a KITP Scholarship under Grant no. NSF PHY05-51164 (JL). Simulations were run using XSEDE resources provided by NICS under Grant No. TG-PHY100053.

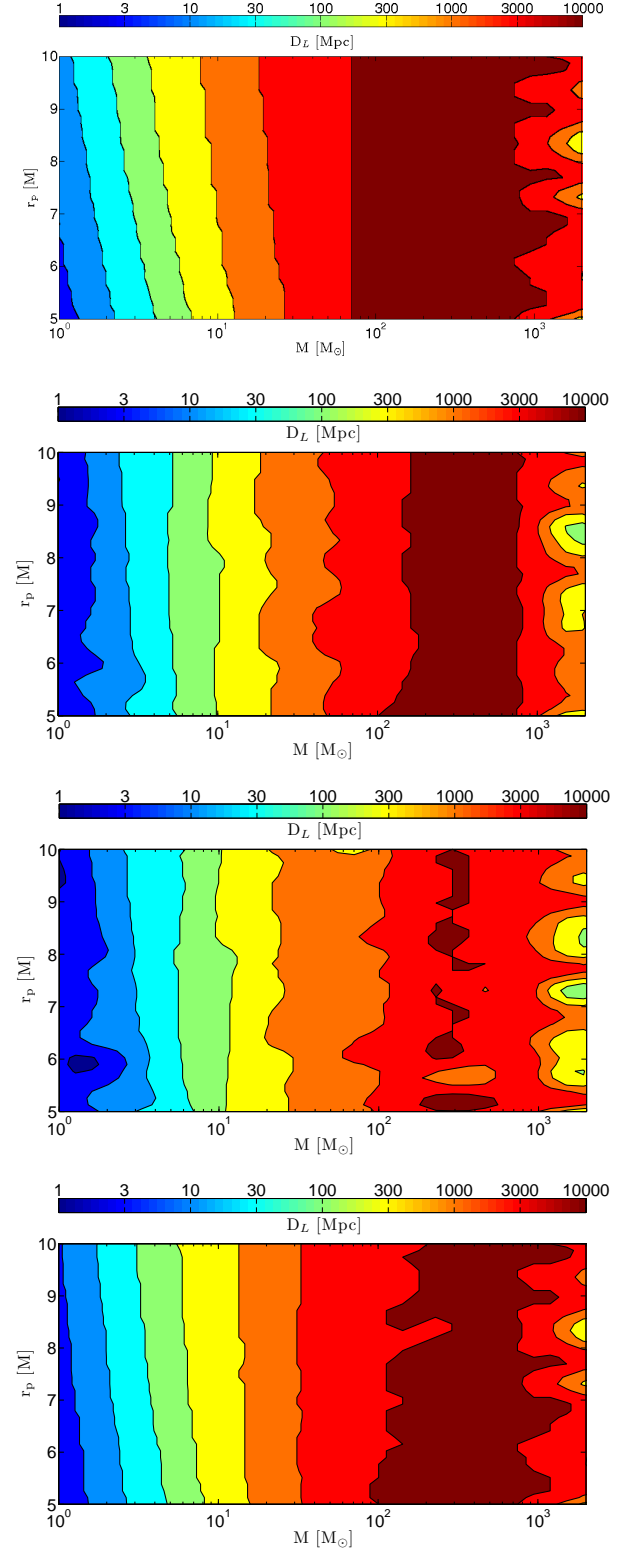


FIG. 16: Contours of horizon distance as a function of rest mass  $M$  and pericenter separation  $r_p$  for Advanced LIGO using, from top to bottom, an optimal filter, sine-Gaussian templates, ringdown templates, and a power-stacking search. The mass ratio is  $q = 1$ .



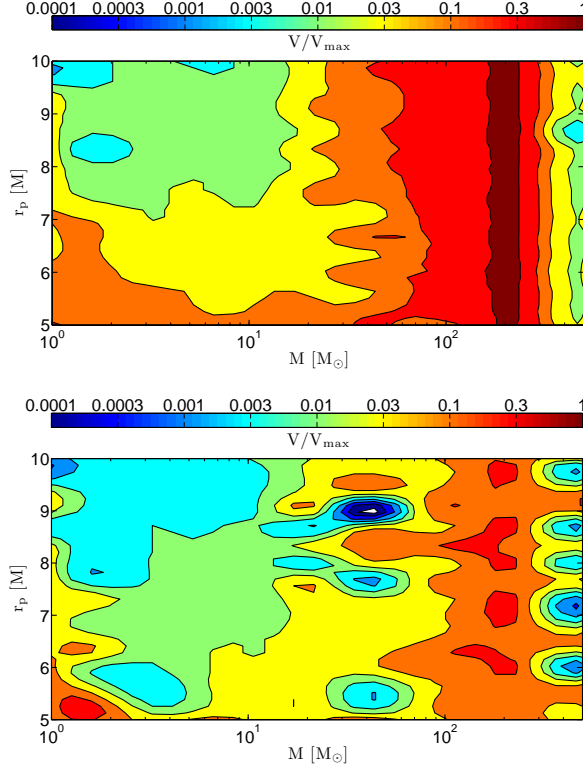


FIG. 17: Contours of detection probability as a function of rest mass  $M$  and pericenter separation  $r_p$  for Enhanced LIGO for a source inside the optimal filtering distance horizon, using sine-Gaussian (top) and ringdown (bottom) templates. The mass ratio is  $q = 1$ .

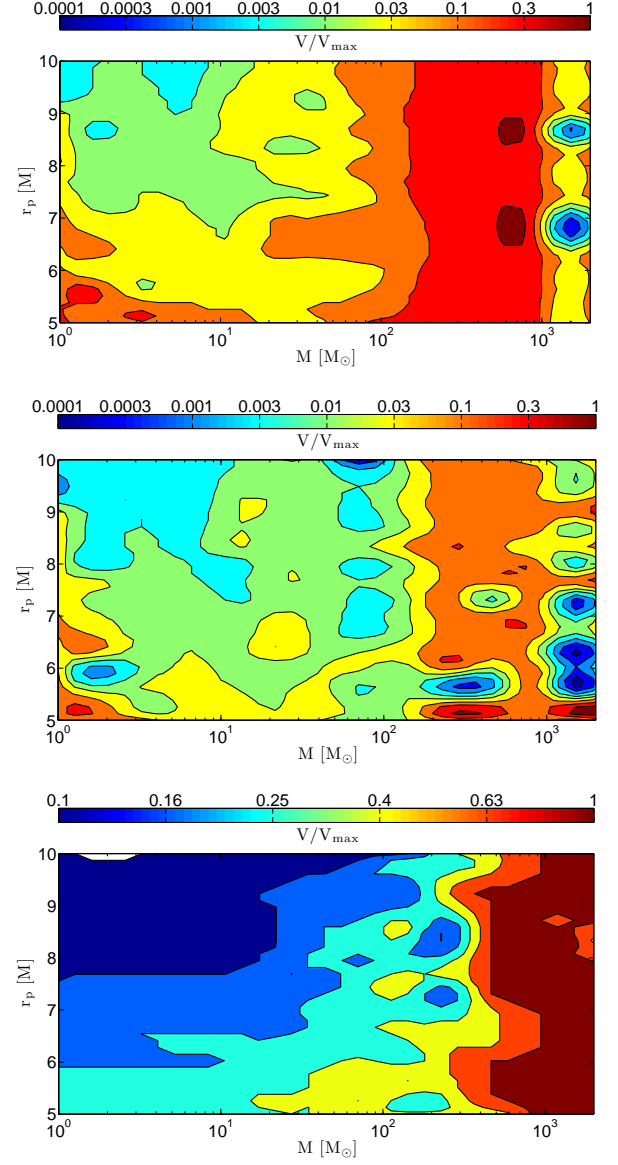


FIG. 18: Contours of detection probability as a function of rest mass  $M$  and initial pericenter separation  $r_p$  for Advanced LIGO for a source inside the optimal-filtering horizon distance, using sine-Gaussian (top) and ringdown (middle) templates and a power-stacking search (bottom). The mass ratio is  $q = 1$ . Note the different scale in the bottom figure.



- 
- [1] A. A. Abramovici *et al.*, Science **256**, 325 (1992).
- [2] B. Caron *et al.*, Class.Quant.Grav. **14**, 1461 (1997).
- [3] B. Willke *et al.*, Class.Quant.Grav. **19**, 1377 (2002).
- [4] LCGT Collaboration, M. Ohashi, Prog.Theor.Phys.Suppl. **190**, 335 (2011).
- [5] C. Hopman and T. Alexander, Astrophys. J. Lett. **645**, L133 (2006), arXiv:astro-ph/0603324.
- [6] R. M. O’Leary, B. Kocsis, and A. Loeb, Mon. Not. R. Astron. Soc. **395**, 2127 (2009), arXiv:0807.2638 [astro-ph].
- [7] B. Kocsis and J. Levin, Phys. Rev. D **85**, 123005 (2012).
- [8] U. Keshet, C. Hopman, and T. Alexander, Astrophys. J. Lett. **698**, L64 (2009).
- [9] A. C. Fabian, J. E. Pringle, and M. J. Rees, Mon. Not. R. Astron. Soc. **172**, 15P (1975).
- [10] D. Pooley *et al.*, Astrophys. J. Lett. **591**, L131 (2003), arXiv:astro-ph/0305003.
- [11] W. H. Lee, E. Ramirez-Ruiz, and G. van de Ven, Astrophys. J. **720**, 953 (2010), 0909.2884.
- [12] S. R. Kulkarni, P. Hut, and S. McMillan, Nature **364**, 421 (1993).
- [13] S. Sigurdsson and L. Hernquist, Nature **364**, 423 (1993).
- [14] S. F. P. Zwart and S. L. W. McMillan, Astrophys. J. Lett. **528**, L17 (2000).
- [15] R. M. O’Leary, F. A. Rasio, J. M. Fregeau, N. Ivanova, and R. O’Shaughnessy, Astrophys. J. **637**, 937 (2006), arXiv:astro-ph/0508224.
- [16] S. Aarseth, (2012), 1202.4688.
- [17] B. W. Murphy, H. N. Cohn, and P. M. Lugger, Astrophys. J. **732**, 67 (2011), 1205.1049.
- [18] J. D. Dull *et al.*, Astrophys. J. **481**, 267 (1997).
- [19] E. Pfahl, S. Rappaport, and P. Podsiadlowski, Astrophys. J. **573**, 283 (2002), arXiv:astro-ph/0106141.
- [20] J. Grindlay, S. Portegies Zwart, and S. McMillan, Nature Physics **2**, 116 (2006), arXiv:astro-ph/0512654.
- [21] D. Clausen, S. Sigurdsson, and D. F. Chernoff, (2012), 1210.8153.
- [22] L. Wen, Astrophys. J. **598**, 419 (2003), astro-ph/0211492.
- [23] M. C. Miller and D. P. Hamilton, Astrophys. J. **576**, 894 (2002).
- [24] F. Antonini and H. B. Perets, Astrophys. J. **757**, 27 (2012).
- [25] T. A. Thompson, Astrophys. J. **741**, 82 (2011), 1011.4322.
- [26] S. Naoz, B. Kocsis, A. Loeb, and N. Yunes, ArXiv e-prints (2012), 1206.4316.
- [27] B. Katz and S. Dong, ArXiv e-prints (2012), 1211.4584.
- [28] P. C. Peters and J. Mathews, Phys. Rev. **131**, 435 (1963).
- [29] P. C. Peters, Phys. Rev. **136**, B1224 (1964).
- [30] M. Turner, Astrophys. J. **216**, 610 (1977).
- [31] B. D. Metzger and E. Berger, Astrophys. J. **746**, 48 (2012), 1108.6056.
- [32] T. Piran, E. Nakar, and S. Rosswog, ArXiv e-prints (2012), 1204.6242.
- [33] D. Kasen, Radioactively powered transients from compact object mergers, 2012, work presented at KITP ‘Rattle and Shine’ conference.
- [34] E. Nakar and T. Piran, Nature **478**, 82 (2011), 1102.1020.
- [35] K. Kyutoku, K. Ioka, and M. Shibata, (2012), 1209.5747.
- [36] B. C. Stephens, W. E. East, and F. Pretorius, Astrophys. J. Lett. **737**, L5 (2011), 1105.3175.
- [37] W. E. East, F. Pretorius, and B. C. Stephens, Phys. Rev. D **85**, 124009 (2012).
- [38] W. E. East and F. Pretorius, Astrophys. J. Lett. **760**, L4 (2012), 1208.5279.
- [39] S. Rosswog, T. Piran, and E. Nakar, ArXiv e-prints (2012), 1204.6240.
- [40] E. Berger, Astrophys. J. **722**, 1946 (2010), 1007.0003.
- [41] R. P. Church, A. J. Levan, M. B. Davies, and N. Tanvir, Mon. Not. Roy. Astron. Soc., 355 (2011), 1101.1088.
- [42] J. D. M. Dewi, P. Podsiadlowski, and O. R. Pols, Mon. Not. Roy. Astron. Soc. **363**, L71 (2005), arXiv:astro-ph/0507628.
- [43] J. P. Norris, N. Gehrels, and J. D. Scargle, Astrophys. J. **735**, 23 (2011), 1101.1648.
- [44] W. F. Domainko, Astron. and Astrophys. **533**, L5 (2011), 1106.4397.
- [45] E. Troja, S. Rosswog, and N. Gehrels, Astrophys. J. **723**, 1711 (2010).
- [46] LIGO Collaboration, Virgo Collaboration, J. Abadie *et al.*, Phys.Rev. **D85**, 082002 (2012), 1111.7314.
- [47] B. Kocsis, M. E. Gaspar, and S. Marka, Astrophys. J. **648**, 411 (2006).
- [48] F. Pretorius and D. Khurana, Class. Quantum Grav. **24**, S83 (2007), arXiv:gr-qc/0702084.
- [49] I. Hinder, F. Herrmann, P. Laguna, and D. Shoemaker, Phys. Rev. D **82**, 024033 (2010), arXiv:0806.1037 [gr-qc].
- [50] J. Healy *et al.*, Phys. Rev. Lett. **102**, 041101 (2009), arXiv:0807.3292 [gr-qc].
- [51] R. Gold and B. Brügmann, Class. Quantum Grav. **27**, 084035 (2010), arXiv:0911.3862 [gr-qc].
- [52] R. Gold, S. Bernuzzi, M. Thierfelder, B. Bruegmann, and F. Pretorius, (2011), 1109.5128.
- [53] R. Gold and B. Bruegmann, (2012), 1209.4085.
- [54] J. G. Baker *et al.*, Phys. Rev. D **78**, 044046 (2008), arXiv:0805.1428 [gr-qc].
- [55] B. J. Kelly, J. G. Baker, W. D. Boggs, S. T. McWilliams, and J. M. Centrella, Phys. Rev. D **84**, 084009 (2011), arXiv:1107.1181 [gr-qc].
- [56] K. Glampedakis, S. A. Hughes, and D. Kennefick, Phys.Rev. **D66**, 064005 (2002), gr-qc/0205033.
- [57] S. Babak, H. Fang, J. R. Gair, K. Glampedakis, and S. A. Hughes, Phys.Rev. **D75**, 024005 (2007), gr-qc/0607007.
- [58] C. F. Sopuerta and N. Yunes, Phys.Rev. **D84**, 124060 (2011), 1109.0572.
- [59] N. Yunes, C. F. Sopuerta, L. J. Rubbo, and K. Holley-Bockelmann, Astrophys.J. **675**, 604 (2008), 0704.2612.
- [60] R. Ruffini and M. Sasaki, Progress of Theoretical Physics **66**, 1627 (1981).
- [61] P. Kalmus, K. C. Cannon, S. Márka, and B. J. Owen, Phys. Rev. D **80**, 042001 (2009).
- [62] K. Hurley *et al.*, Mon. Not. R. Astron. Soc. **403**, 342 (2010).
- [63] B. P. Abbott *et al.*, Astrophys. J. **715**, 1438 (2010).
- [64] J. Abadie *et al.*, Astrophys. J. **715**, 1453 (2010).
- [65] J. N. Goldberg, A. J. MacFarlane, E. T. Newman, F. Rohrlich, and E. C. G. Sudarshan, J. Math. Phys. **8**, 2155 (1967).
- [66] W. E. East, F. Pretorius, and B. C. Stephens, Phys. Rev. D **85**, 124010 (2012).

- [67] T. Damour, B. R. Iyer, and B. S. Sathyaprakash, Phys. Rev. D **57**, 885 (1998), arXiv:gr-qc/9708034.
- [68] J. Levin, S. T. McWilliams, and H. Contreras, Class. Quantum Grav. **28**, 175001 (2011).
- [69] K. S. Thorne, in *300 Years of Gravitation* (Cambridge University Press, Cambridge, 1987).
- [70] T. Damour, B. R. Iyer, and B. S. Sathyaprakash, Phys. Rev. D **62**, 084036 (2000), arXiv:gr-qc/0001023.
- [71] E. P. Mazets *et al.*, Astrophys. J. **680**, 545 (2008).
- [72] S. T. McWilliams, B. J. Kelly, and J. G. Baker, Phys. Rev. D **82**, 024014 (2010), arXiv:1004.0961 [gr-qc].
- [73] A. Buonanno and T. Damour, Phys. Rev. D **59**, 084006 (1999), arXiv:gr-qc/9811091.
- [74] D. Bini and T. Damour, (2012), 1210.2834.